ORIGINAL PAPER

Primary and potential secondary risks of landslide outburst floods

Yunjian Gao[1,2] · Lee Chack Fan[3] · Jianhui Deng[1] · Siyuan Zhao[1] · Wen Dai[4] · Jun Zhu[5] · Zhiliang He[1] · Zhongkang Yang[1] · Stuart N. Lane[2]

Abstract

Outburst floods triggered by breaching of landslide dams may cause severe loss of life and property downstream. Accurate identification and assessment of such floods, especially when leading to secondary impacts, are critical. In 2018, the Baige landslide in the Tibetan Plateau twice blocked the Jinsha River, eventually resulting in a severe outburst flood. The Baige landslide remains active, and it is possible that a breach happens again. Based on numerical simulation using a hydrodynamic model, remote sensing, and field investigation, we reproduce the outburst flood process and assess the hazard associated with future floods. The results show that the hydrodynamic model could accurately simulate the outburst flood process, with overall accuracy and Kappa accuracy for the flood extent of 0.956 and 0.911. Three future dam break scenarios were considered with landslide dams of heights 30 m, 35 m, and 51 m. The potential storage capacity and length of upstream flow back up in the upstream valley for these heights were $142 \times 10^6 m^3/32$ km, $182 \times 10^6 m^3/40$ km, and $331 \times 10^6 m^3/50$ km. Failure of these three dams leads to maximum inundation extents of 0.18 km², 0.34 km², and 0.43 km², which is significant out-of-bank flow and serious infrastructure impacts. These results demonstrate the seriousness of secondary hazards associated with this region.

Keywords Outburst flood · Baige landslide · BASEMENT model · Remote sensing interpretation · Flood disasters assessment

✉ Yunjian Gao
gaoyunjiansu@163.com

1   State Key Laboratory of Hydraulics and Mountain River Engineering, College of Water Resource & Hydropower, Sichuan University, No. 24 South Section 1, Yihuan Road, Chengdu 610065, Sichuan, China

2   Institute of Earth Surface Dynamics (IDYST), University of Lausanne, 1015 Lausanne, Switzerland

3   Ningbo Institute of Technology, Zhejiang University, Ningbo 315100, China

4   School of Geographical Sciences, Nanjing University of Information Science & Technology, Nanjing 210044, China

5   Key Laboratory of Mountain Hazards and Earth Surface Process, Institute of Mountain Hazards and Environment, Chinese Academy of Sciences (CAS), Chengdu 610041, China

1 Introduction

Landslide damming of laterally confined rivers is reported with increasing frequency (Knapp et al. 2018; Fan et al. 2019; Ermini and Casagli 2003; Chen et al. 2013; Guo et al. 2021). If these dams breach, the subsequent outburst floods may induce catastrophic casualties and major damage to property downstream (Fan et al. 2020c; Bonnard 2006; Wang et al. 2021). The Tibetan Plateau, European Alps, and Western North American mountainous regions are those where landslide dam breaches are most commonly reported (Knapp et al. 2018; Fan et al. 2019). Examination of previous dam failures shows that globally about 80 to 90% fail within the first year of formation (Costa and Schuster 1988b, a; Fan et al. 2020c). Fan et al. (2020c) record more than 410 landslide dams around the world, of which about 80% failed in less than one year. Ermini and Casagli (2003) recorded more than 350 landslides dams worldwide, either rainfall or earthquake triggered with 80% and 57% of them breaching and triggering a flood disaster, respectively. In China, giant landslide-dammed events are most common in mountainous areas. The Yigong landslide is a good example, feeding sediment into the Zhamunong tributary and blocking the Yigong River with a barrier of about 50 m to 80 m height in 1901 and 2000 (Zhou et al. 2016; Shang et al. 2003; Xu et al. 2012). Subsequently, the outburst flood travelled over 500 km south into India (Delaney and Evans 2015), it threatened about 4000 people downstream, and the economic loss from the flooding was about $169 000 US dollars (Shang et al. 2005; Evans and Delaney 2011).

On October 10, and November 3, 2018, two successive landslides occurred at Baige Village, Jiangda County, Tibetan Autonomous Region, P.R. China (Wu et al. 2019; Yang et al. 2019; Wang et al. 2020; Li et al. 2020a, b; Ding et al. 2021; An et al. 2021; Zhang et al. 2020). They delivered about $18.7 \times 10^6 \mathrm{m}^3$ and $6.3 \times 10^6 \mathrm{m}^3$ of sediment, blocking the Jinsha River and forming landslide-dammed lakes (Chen et al. 2021a, b; Ouyang et al. 2019). After each dam formed, the barrier lake breached and the outburst floods caused flood disaster damage downstream. The landslide dams blocked the Jinsha River for 44 h and 13 days, respectively. The dam heights were 47 m and 72 m, and the subsequent lake that formed extended 45 km and 70 km, and the peak storage capacity reached $0.29 \times 10^9 \mathrm{m}^3$ and $0.58 \times 10^9 \mathrm{m}^3$. There was significant infrastructure damage, and the whole of Boluo Town was inundated (Chen et al. 2021a, b; Gao et al. 2021; Xiong et al. 2020). With the dam break, the river discharge increased to 10,000 $\mathrm{m}^3\mathrm{s}^{-1}$ and 31,000 $\mathrm{m}^3\mathrm{s}^{-1}$, respectively. The outburst flood reached 670 km downstream, with roads, houses, farms, and bridges damaged; for example, 18 bridges were affected and collapsed (Zhang et al. 2021; Liu et al. 2020a, b). Fortunately, the two flood events did not induce casualties due to sufficient time between breaches and inundation, so that warnings could be issued.

The rear edge of the Baige landslide has continued to deform since the first two landslide events, and there is a high probability of further secondary hazards involving dam formation and breaching (Chen et al. 2021a, b; Fan et al. 2020a, b). Although future outburst flood hazard assessment for the Baige landslide is essential, most of the attention has been on post-outburst floods. This work has struggled to quantify post-flood impacts using remote sensing (Liu et al. 2020a, b; Yang et al. 2021), notably because of poor image quality. The one-dimensional HEC–RAS hydraulic model has been used to simulate the flood (Fan et al. 2020d; Gao et al. 2021), but its precision is insufficient because it relies on cross section density and struggles to reproduce spatial patterns of inundation when there is substantial flux of water on the floodplain rather than in the channel. Improvements in hydraulic modelling are needed, to allow for a better assessment of inundation patterns

in two dimensions. The aim of this paper is to develop a coupled approach to landslide dam failure and two-dimensional hydraulic modelling for assessing downstream flood risk, applied here to the Baige landslide.

2 Overview of the landslide and the study area

The Baige landslide is located at Boluo Town, Jiangda County, in the Tibet Autonomous Region, China (31.082336°N, 98.704722°E). It periodically dams the Jinsha River of the Tibetan Plateau. It is in the Jinsha River suture zone and is associated with strong tectonic activity; the tectonic setting of the area is quite complex; faults and folds are well developed. Proterozoic, Carboniferous, and Triassic strata are the major rocks in the study area. The major faults in the area generally strike NW–SE, and the Boluo–Muxie Fault is the nearest one to the slides which strike N30° W and dip 50 to 70° to SW. The fault is 146 km long, and its fault belt is 100 to 300 m wide. The Jinsha River undercuts the plateau forming a V-shaped valley which allows for the Baige landslide to readily block the river.

According to field investigations and remote sensing, a total of 41 towns were affected by two Baige outburst floods, with a maximum inundated area of about 102 km^2 in the second flood. This paper focuses on a 9 km reach at Zhubalong Town in the Jinsha River in Batang County (Fig. 1). Zhubalong Town was selected for the focus as it is a city of considerable importance in terms of infrastructure**.** It was 180 km downstream of the dam but still experienced serious flood impacts. The study reach is representative of other reaches impacted by the floods in that it comprises a wide floodplain.

3 Overall methodology and data sources

Figure 2 provides an overview of the outburst flood analysis presented in the paper. It is based upon coupling and upstream analysis of likely dam breach risk and impact in terms of an extreme discharge event with a two-dimensional hydrodynamic model, applied here to a downstream reach at Zhubalong Town. It focuses on the largest of the 2018 events, which provides for validation of the analysis. Then, the hydrodynamic model is applied to determine the inundation for possible future dam breach scenarios. This approach, whilst determining locally specific data for model application and calibration is generic and therefore of wider use.

3.1 Data sources

The flood hazard assessment in this work was based upon numerical simulation, satellite imagery, Digital Elevation Model (DEM) data, and hydrological information. First, the PlanetScope satellite imagery data were obtained from the "Planet Developer Resource Centre (Planet Explorer)". PlanetScope data are based upon approximately 130 satellites and can image the entire land surface of the Earth daily. PlanetScope images are approximately 3 m or 3.7 m per pixel resolution and are generally divided into 4 bands (B, G, R, and NIR) (Table 1). These data were used to identify maximum flood extent during the event (see below). The flood has a clear signature in terms of maximum extent due to extensive fine sediment deposition. Second, the ALOS (Advanced Land Observing Satellite) DEM data, produced using ALOS panchromatic three-line images, were used for the
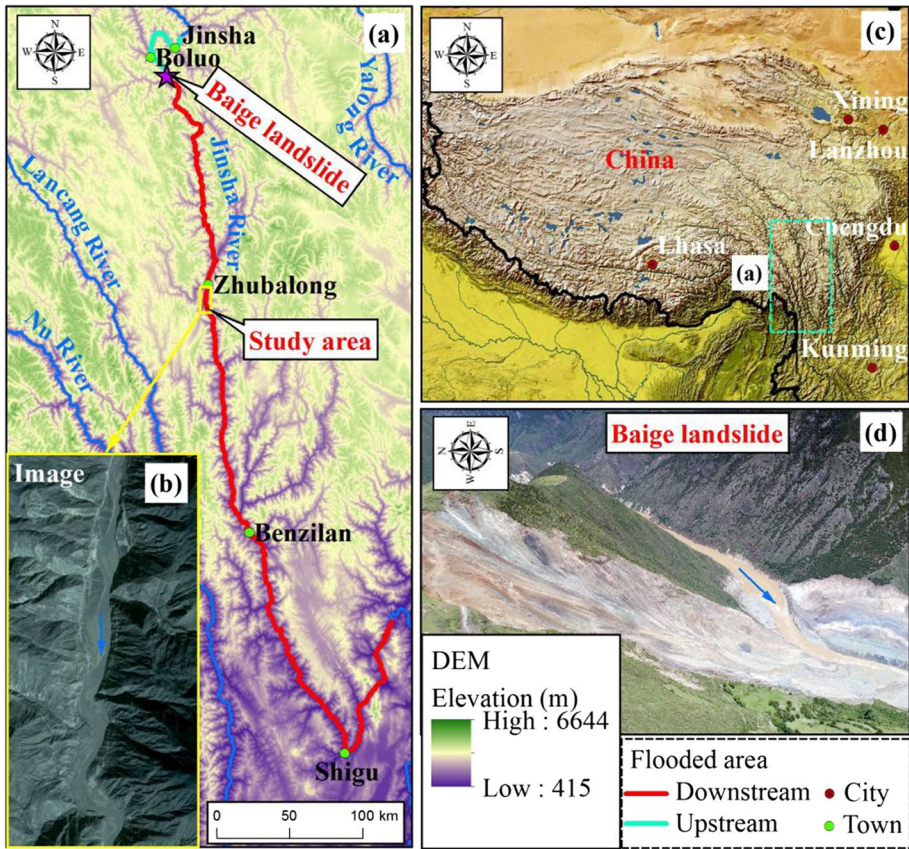
Fig. 1 Location of the Baige landslide and the study area. **a**, **c** Baige landslide flood impact extent. **b** Study area satellite image. **d** Baige landslide aerial image

hydrodynamic model. These data have a spatial resolution of 5 m and were obtained from the Geographical Survey Institute of Japan. Finally, discharge data were provided from the Batang gauging station in the Jinsha River (Fig. 3), providing reliable real-time monitoring data (Gao et al. 2021; Chen et al. 2021a, b). A peak discharge of 20,900 m^3s^{-1} was recorded during the second flood (Fig. 3).

3.2 Methods

3.2.1 Remote sensing interpretation

The outburst floods occurred on 12 October and 13 November 2018. 7 October and 15 November 2018 were selected as dates with cloud-free imagery from before to after the two events; as the second flood was larger, 15 November data are likely representative of this event. The imagery records the extent of the flood's impact, and it can be used to distinguish between inundated and non-inundated zones (vegetation-covered
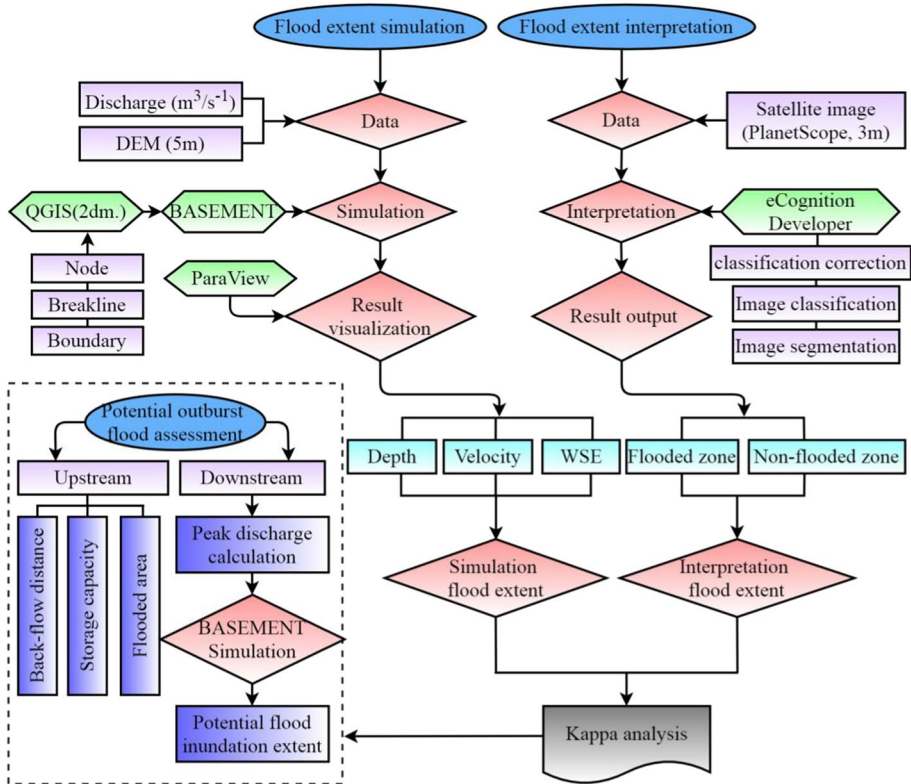
Fig. 2 Flow chart of the outburst flood analysis

Table 1 Satellite image and DEM data source

Data	Acquisition time	Spatial resolution	Data source
PlanetScope (satellite)	2018.10.07	3 m	Planet developer resource centre (https://account.planet.com/)
	2018.10.25	3 m	
	2018.11.15	3 m	
DEM	–-	5 m	ALOS

zone). The maximum inundated extent impacted by the outburst floods was mapped by comparing imagery from before to after the flood. The eCogition Developer version 9.0 software was used to conduct the remote sensing. First, the RGB bands were displayed (Fig. 4a). Second, a multi-resolution segmentation algorithm (MESA; Benz et al. 2004) was applied at the pixel scale. This algorithm starts with individual pixels and merges them with adjacent pixels according to their homogeneity. The MRSA was applied with
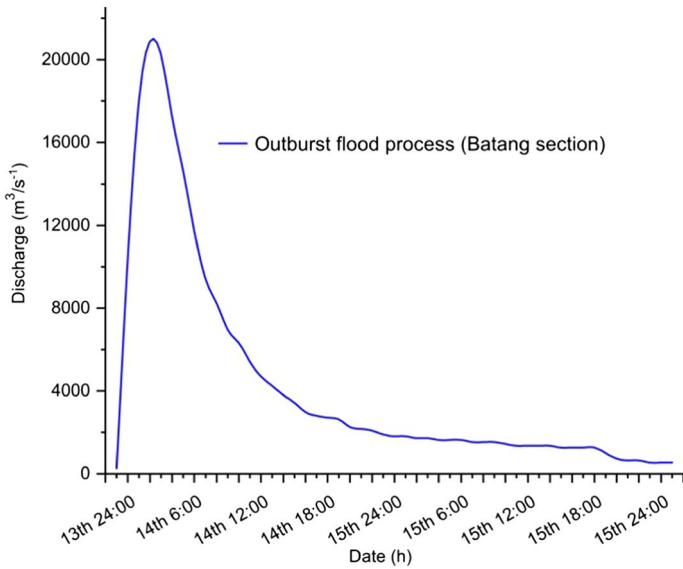
Fig. 3 Discharge hydrograph measured for the Batang County reach
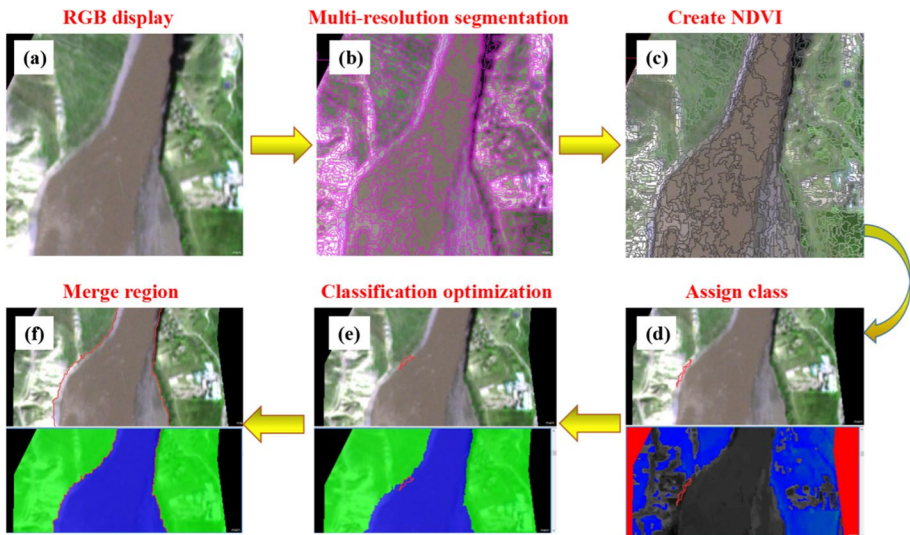

**Fig. 4** Method to delineate flood inundation extent using remote sensing

a scale parameter of 25 m (Fig. 4b). Third, the Normalised Difference Vegetation Index (NDVI) was determined (Fig. 4c):

$$\text{NDVI} = \frac{\text{NIR}_{\text{mean}} - R_{\text{mean}}}{\text{NIR}_{\text{mean}} + R_{\text{mean}}} \tag{1}$$

The NDVI is used to detect vegetation growth state, vegetation coverage and eliminate partial radiation error. It reflects well on the characteristics of plant distribution and is easy to distinguish from inundated zones. Fourth, the imagery was classified into vegetation zones (non-inundated zone) and inundated zones based upon a threshold value of the NDVI. In this study, the NDVI of the vegetation zones was between 0.16 and 1.0 (Fig. 4d). Fifth, a manual classification was undertaken to provide validation data got assessing the automated classification (Fig. 4e). Sixth, the classes were merged to produce non-inundated zones (vegetation-covered zones) and inundated zones (Fig. 4f).

3.2.2 Determination of potential landslide dam height

The secondary failure and landslide-dammed lake risk of the Baige landslide are high with the continuous deformation of the landslide edge and rear (Chen et al. 2021a, b; Zhang et al. 2021; Zhou et al. 2022). Crack zones have been identified in several detailed field investigations, which implies that the area of landslide potential high-risk zones can be determined (Fig. 5a–e). A deep displacement monitoring instrument (SINCO) was used to detect slope deformation and to identify the landslide sliding surface with manual measurement, once per month on average. The total monitoring time was from June 2019 to December 2021. The
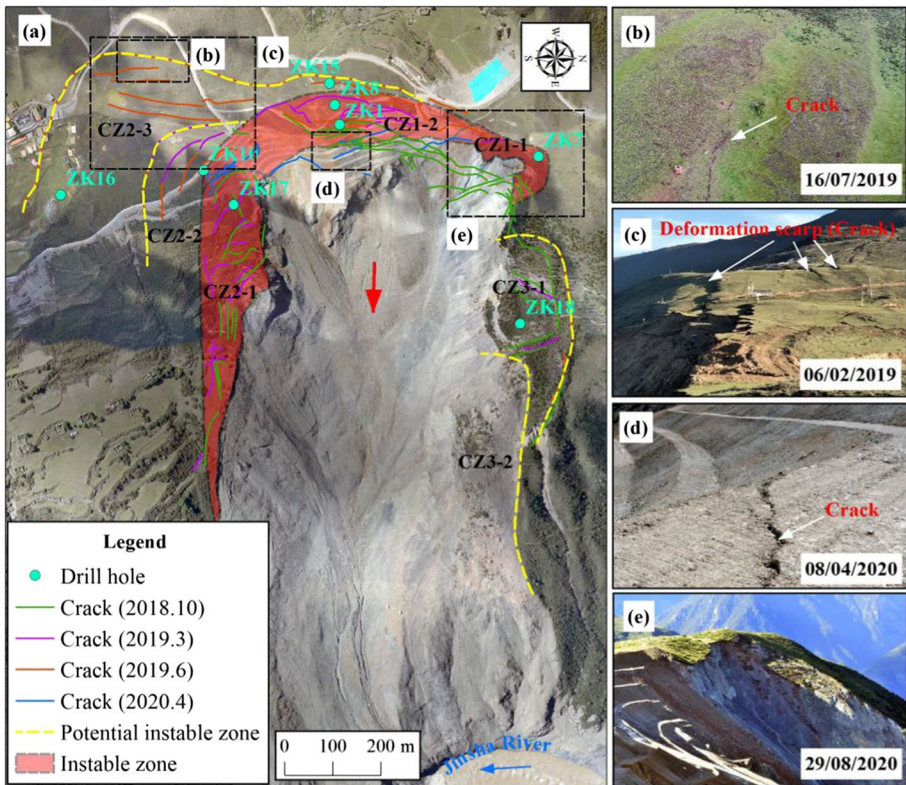
Fig. 5 Deformation characteristics of the Baige landslide. **a** Deformation area and crack distribution of the Baige landslide edge and rear. **b** Boundary crack of the Baige landslide rear. **c** Historical deformation scarp. **d** Crack propagation in engineering cutting area. **e** Severe deformation zone

potential landslide volume was calculated based upon surface area and the estimated depth to the shear plane.

The potential landslide dam height was determined based upon the landslide volume, dam shape, and the shape of the deposit (dam breach deposit) that formed downstream from the breach. For the two 2018 breaches, distinctive dam breach deposit shapes were identified (Fig. 6a). These deposits then determined the required landslide mass needed to create a landslide dam during future landslide failures (Fig. 6a). The landslide dam shape, especially the back and front slope, could be extracted to restrict the crest of the dam assuming that the landslide accumulation process operates in a similar way (Fig. 6b, c). Using this approach, it was possible to identify landslide dam heights at risk of future breaching.

3.2.3 Hydrodynamic model

The simulation of inundation was based upon the shallow water equations which solve for continuity (conservation of mass or volume) and momentum to calculate the propagation of shallow water flows over natural topography. There are four aspects that must be considered: (1) the form of the terms use to describe conservation of mass and momentum; (2) numerical solution of the associated partial differential equations; (3) parameterization (as shown in Table 2), notably of flow resistance which is generally the parameter that has most impact on flood inundation prediction; and (4) the description of channel and floodplain geometry (Lane 1998; Worni et al. 2013).

The two-dimensional numerical model BASEMENT (Zischg et al. 2018) was used to investigate and simulate flood inundation in the study reach. BASEMENT has been designed as a tool for application to the study of flood inundation and coupled water–sediment processes (Lala et al. 2018). The 2D shallow water Eqs. (2) through (4) are solved with an explicit finite-volume method on an unstructured mesh (Worni et al. 2013). The water depth h and specific discharges ($q = uh$, $r = vh$) are the primary variables in the coordinate directions.

$$\frac{\partial h}{\partial t} + \frac{\partial (uh)}{\partial x} + \frac{\partial (vh)}{\partial y} = 0 \qquad (2)$$
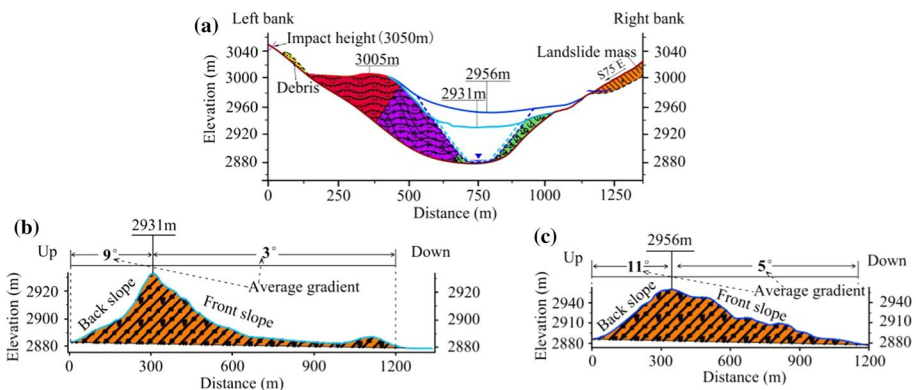
Fig. 6 a Landslide dam cross sections and dam breach deltas for the two flood events. b Longitudinal profile for the first 2018 event. c Longitudinal profile for the second 2018 event

Table 2 Parameters of the BASEMENT model simulation outburst flood

Gravity (ms^{-2})	Viscosity (m^{-2} s)	Reynolds number (kg/m^3)	Boundary condition		Friction (sm$^{-1/3}$)	Total run time (s)
9.8	0.000001	5000	Inlet	Outlet	0.03	46,800 (actual process)
			Data: discharge Slope:3 (per mill)	Data: the normal depth Slope:3 (per mill)		

$$\frac{\partial}{\partial t}(hu) + \frac{\partial}{\partial x}\left(hu^2 + \frac{1}{2}gh^2\right) + \frac{\partial}{\partial y}(huv) = -gh\frac{\partial Z_B}{\partial x} - \frac{\tau_{Bx}}{\rho} \tag{3}$$

$$\frac{\partial}{\partial t}(hv) + \frac{\partial}{\partial x}(huv) + \frac{\partial}{\partial y}\left(hv^2 + \frac{1}{2}gh^2\right) = -gh\frac{\partial Z_B}{\partial x} - \frac{\tau_{By}}{\rho} \tag{4}$$

where u is the velocity in x direction, v is velocity in y direction, g is the gravitational acceleration, ρ is the fluid density, and Z_B is the bottom elevation. The bed shear stresses (τ_{Bx}, τ_{By}) act in the direction of depth-averaged velocities and are determined using the quadratic resistance law with c_f being the dimensionless friction factor as (5). Flow resistance is generally described by the empirical Strickler (Range: $7 \sim 40$ m$^{1/3}$ s^{-1}) or Manning coefficients (Range: $0.025 \sim 0.143$ m$^{-1/3}$ s) (Vanzo et al. 2021).

$$\tau_{Bx} = \rho\sqrt{u^2 + v^2}u/c_f^2, \quad \tau_{By} = \rho\sqrt{u^2 + v^2}v/c_f^2 \tag{5}$$

Generating an irregular triangle mesh is a fundamental step in the process. DEM data were used to generate the nodes, each with an elevation value. Triangular meshes were generated by using the pre-processing plug-in in QGIS software, as shown in Fig. 7. Finally, with execution of the BASEMENT model, flood data on water depth, velocity, and water surface elevation (WSE) were obtained.

The study area has low forest coverage and housing density, and so, the Manning's friction was set as 0.03 (Chow et al. 1988). The run time of the flood simulation was set as 46,800 s, noting the peak discharge occurred at 10,800 s and that the maximum inundation extent was reached well before the end of this time for the second flood. The boundary condition was set as the stage-discharge curve of Batang County upstream and a normal depth condition downstream. The associated parameters are shown in Table 2.

3.2.4 Accuracy analysis of model predictions

Kappa-based contingency analysis (Cohen 1960) was used to assess the accuracy of the BASEMENT simulation flood result using predicted and observed inundation patterns. The foundation of all accuracy assessments is an error matrix (Fig. 8). With two classes, inundated or not, the error matrix is a 2×2 space (Fig. 8). Here, n_{11} and n_{22} are represented the numbers of cells of consistent wet and consistent dry classes in both the

simulation and the actual results. n_{12} and n_{21} are represented the number of cells of the 'wet versus dry' and the 'dry versus wet' between the simulation and the actual results.

The overall accuracy is identified from Eq. (6) as the sum of the correctly predicted cells divided by the total number of cells (Yu and Lane 2006). However, this statistic takes no account of random level of agreement in the contingency table.

$$\text{Overall accuracy} = \frac{\sum_{i=1}^{k} n_{ii}}{n} \tag{6}$$

Following Cohen (1960), we therefore used Kappa analysis, and a discrete multivariate technique that is used to allow statistical analysis of model performance and to test if one error matrix is different from the actual result (Fig. 6) (Bishop et al. 1975).

$$K = \frac{n \sum_{i=1}^{k} n_{ii} - \left(\sum_{i=1}^{k} n_{i1} + \sum_{j=1}^{k} n_{ij} \right) \times \left(\sum_{i=1}^{k} n_{i2} + \sum_{j=1}^{k} n_{2j} \right)}{n^2 - \left(\sum_{i=1}^{k} n_{i1} + \sum_{j=1}^{k} n_{ij} \right) \times \left(\sum_{i=1}^{k} n_{i2} + \sum_{j=1}^{k} n_{2j} \right)} \tag{7}$$

Equation (7) is essentially expressing the ratio of the observed excess over chance agreement to the maximum possible excess over chance agreement, with $K = 1.0$ at perfect agreement and $K = 0.0$ when observed agreement equals chance agreement (Everitt 1998). Data required for this assessment were based upon the spatial extent of the modelled domain.

3.2.5 Calculation of the potential outburst flood peak discharge

We aimed to quantify how inundation changes as a function of different magnitudes of river valley blockage by the landslides. This needed simulations of outburst flood magnitudes for different dam heights and their attenuation with distance downstream. The peak discharge is the key parameter that determines the submergence range, scour intensity, and the arrival time of floods downstream. Empirical models and hydrological experiments are the main two ways to determine the peak discharge for potential dam breaching (Costa 1985; Costa and Schuster 1988b, a; Costa and Schuster 1991; Walder and O'Connor 1997; Fread 1988; Peng and Zhang 2012; Habib et al. 2014; Li et al. 2021). Empirical models vary in their complexity. For example, Costa's (1985) empirical model only considered dam height (H_d) for calculating peak flow (Q_p), and Costa and Schuster (1988b, a, 1991) only considered dam height (Hd) and barrier lake storage capacity (V_l). Peng and Zhang (2012) proposed an empirical model to calculate peak discharge, which has been successfully applied to the peak discharge calculation of glacier lake and landslide dam outburst flood (Rivas et al. 2015; Shi et al. 2017). The method was based upon a database of 1239 landslide dams, including 257 dams formed during the Wenchuan earthquake on May 12, 2008. The model considered dam height, dam width, dam volume, reservoir storage capacity of barrier lake, and dam erodibility. The model is shown in (7):

$$\frac{Q_p}{g^{1/2} H_d^{5/2}} = \left(\frac{H_d}{h_r} \right)^{-1.371} \left(\frac{V_l^{1/3}}{H_d} \right)^{1.536} e^a \tag{7}$$

where Q_p is the peak discharge at dam burst (m³s⁻¹), H_d is dam height (m), $H_r = 1$ m (Peng and Zhang 2012), V_l is storage capacity of barrier lake (m³), $g = 9.8$ ms⁻¹, and $e = 2.718$,
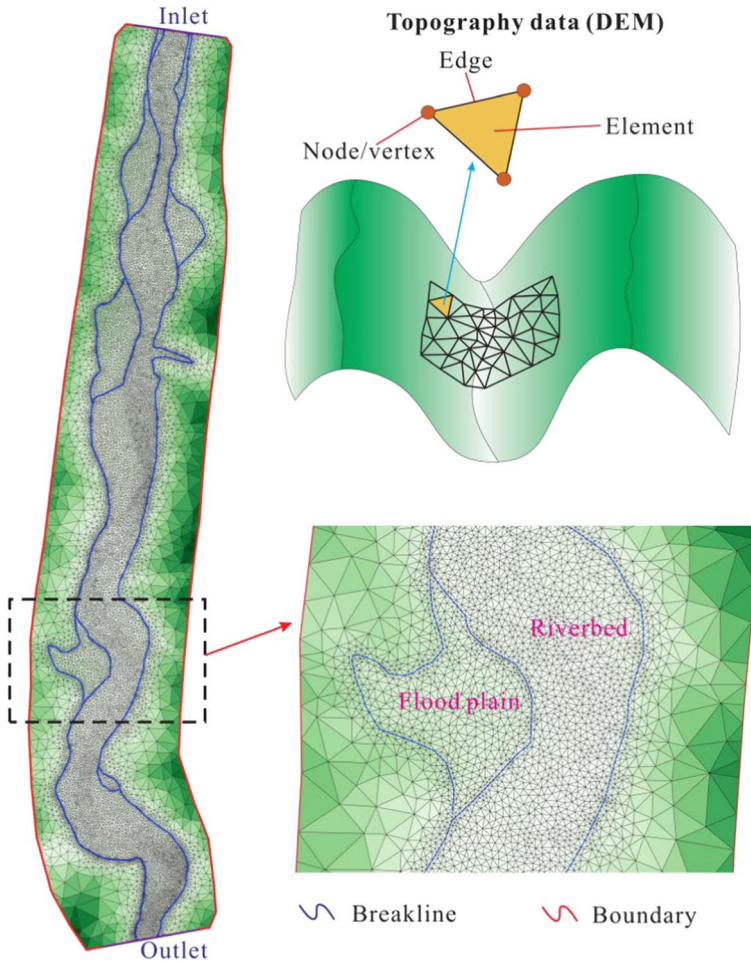
Fig. 7 Irregular triangulation mesh for the BASEMENT flood simulation of the study reach

and a is the dam erodibility parameter which can be divided into three grades: high (1.236), medium (-0.380), and low (-1.615) (Peng and Zhang 2012; Briaud 2008; Hanson and Simon 2001).

The spatial analysis tool in Arcgis 10.2 was used to calculate the storage capacity (V_1) and, as a by-product, the inundation area upstream of different height. The SRTM 30 m spatial resolution DEM data were combined with the dam height to determine the water level height and its intersection with valley topography upstream. This was then overlain on the DEM and, using the cut fill tool of the Arcgis 10.2, allowed the volume of water stored for each dam to be determined. Table 3 illustrates example calculations and also the sensitivity to the dam erodibility parameter a. In this case, we could also back-validate the Peng and Zhang (2012) model against the measured peak discharge calculation for the Baige landslide. For the first outburst flood, and using $a = -0.38$, the landslide dam height

Error matrix		Actual result (Interpretation + field investigation)			Class
		Wet	dry	...	
Simulation result	wet	n_{11}	n_{12}	n_{1j}	1
	dry	n_{21}	n_{22}	n_{2j}	2
	...	n_{i1}	n_{i2}	n_{ij}	k
	Class	1	2	k	...
Kappa value degrees: slight (0.0 - 0.2), fair (0.21 - 0.4), moderate (0.41 - 0.6), substantial (0.61 - 0.8), almost perfect (0.81 - 1.0) (Cohen 1960; Landis and Koch 1977)					

Fig. 8 Error matrix for the Kappa accuracy analysis

was 47 m corresponding to an actual outburst flood peak discharge of 10,000 m^3s^{-1}. Equation (7) gives 9590 m^3s^{-1} for that dam height (47 m). The modelled peak discharge is very close to the actual result, which means Peng and Zhang (2012) model is likely to be effective. For the second outburst flood, the landslide dam height was 72 m corresponding to an actual outburst flood peak discharge of 31,000 m^3s^{-1}. Equation (7) gives 11,347 m^3s^{-1} for that dam height (72 m) with using $a = -0.38$. This model result appears distorted compared with the second peak discharge with the dam height significantly increasing. This deviation likely implies that the dam erodibility parameter (*a*) of this model is not correct. In addition, with the dam height increasing, the estimation of the peak discharge may be too small. However, the dam height for 47 m close to the future potential dam heights considered herein of 30, 35, and 51 m presented a good result.

Whilst this analysis gives the peak discharge at the dam breach, it was also necessary to quantify the evolution of the peak discharge with distance downstream due to attenuation. Data suggested that the shape of the hydrograph retained similarity as the flood wave moved downstream. This allowed the shape of the simulated hydrographs to be scaled to the estimated peak discharge (Figs. 9 and 10).

4 Result

4.1 Validation of flood inundation simulations

Figure 11 shows the estimated active river bed before the second flood and then, after, the latter likely indicating the maximum inundation extent. The remote sensing results suggest that the river was inundated to an extent of 1.5 km^2 (i.e. in the first flood, before the second flood) and that this area increased by 1.6 km^2 in the second flood, such that the total flooded area in the study area is 3.1 km^2. The remote sensing results are used to define the actual flooded area.

Figure 12 superimposes the modelled and predicted inundation and is visually encouraging. The modelled result is in good accordance with the actual result suggesting that the data sources used, and the model parameterization are appropriate. This was confirmed quantitatively with an overall accuracy reaches of 0.956 and a Kappa value of 0.911. Figure 13 confirms a qualitatively good agreement between the measured and the modelled water depths. Mismatches in this figure are likely to reflect inaccuracies in the DEM data and local inconsistencies relating to minor topographical details. The spatial resolution is a significant difference between the DEM data (30 m) and the imagery data (3 m) which may also cause the mismatches.

4.2 Potential landslide dam heights

Investigation and monitoring results show that CZ1-1, CZ1-2, and CZ2-1 were at the highest risk of potential failure (Fig. 5a). Their volumes were about 0.8×10^6m^3, 0.8×10^6m^3, and 3.3×10^6m^3. In addition, there is about 1.0×10^6m^3 of landslide debris residue in the landslide groove created from the last landslide event. Although the volume of potential material (total 5.9×10^6m^3) is lower than for the past two landslide events, its potential hazards will likely be similar and so potentially serious because the breach of the last landslide dam was only small in size. Notably, CZ1-1, CZ1-2, and CZ2-1 are the highest risk zones now. The crack zone boundary is further up-slope, and the extent of potential slope instability may be bigger (Fig. 5).

Based on the shape of the 2018 dams, the dam breach deposit shape, and potential landslide volume, the potential dam height can be calculated. Figure 14 shows three scenarios for potential landslide failures in terms of the high-risk zone covering 'CZ1-1', 'CZ1-1 + CZ2-1', and 'CZ1-1 + CZ1-2 + CZ2-1'. The three scenarios are as follows: 'CZ1-1' is likely the first failure because of the highest risk; CZ1-1 and CZ2-1 ('CZ1-1 + CZ2-1') are likely simultaneous start-ups considering the most severe deformation; CZ1-1, CZ1-2, and CZ2-1 ('CZ1-1 + CZ1-2 + CZ2-1') are likely simultaneous failures because the crack zones are interconnected (Fig. 5). The associated landslide failure volumes are 1.3×10^6m^3, 2.6×10^6m^3, and 5.9×10^6m^3 and form landslide dams 30 m, 35 m, and 51 m high, respectively (Fig. 14).

4.3 Flood simulations for the November 2018 event

The main three simulation outputs were depths, velocities, and the maximum flood inundated area of the outburst flood. The total simulation time is 46,800 s, which has been divided into four steps that included 10,800 s, 21,600 s, 324,00 s, and 43,200 s for

Table 3 Peng and Zhang (2012) model validation for potential peak discharge of the dam breaching

|	Dam height (H_d, m)	g	Storage capacity (V_d, m³)	E	a	Peak discharge (m³/s⁻¹)
Measured outburst flood peak discharge for the first and second 2018 events	47	9.8	290,000,000	2.718	−1.615	2794
	47	9.8	290,000,000	2.718	−0.38	9590
	47	9.8	290,000,000	2.718	1.236	48,331
	72	9.8	580,000,000	2.718	−1.615	3300
	72	9.8	580,000,000	2.718	−0.38	11,347
	72	9.8	580,000,000	2.718	1.236	57,088
Actual peak discharge: 10,000 m³/s⁻¹ (first event) and 31,000 m³/s⁻¹ (second event)						
Potential outburst flood peak discharge	30	9.8	142,000,000	2.718	−1.615	2326
	35	9.8	182,000,000	2.718	−1.615	2467
	51	9.8	331,000,000	2.718	−1.615	2918
	30	9.8	142,000,000	2.718	−0.38	7928
	35	9.8	182,000,000	2.718	−0.38	8440
	51	9.8	331,000,000	2.718	−0.38	9965
	30	9.8	142,000,000	2.718	1.236	40,262
	35	9.8	182,000,000	2.718	1.236	42,668
	51	9.8	331,000,000	2.718	1.236	50,468
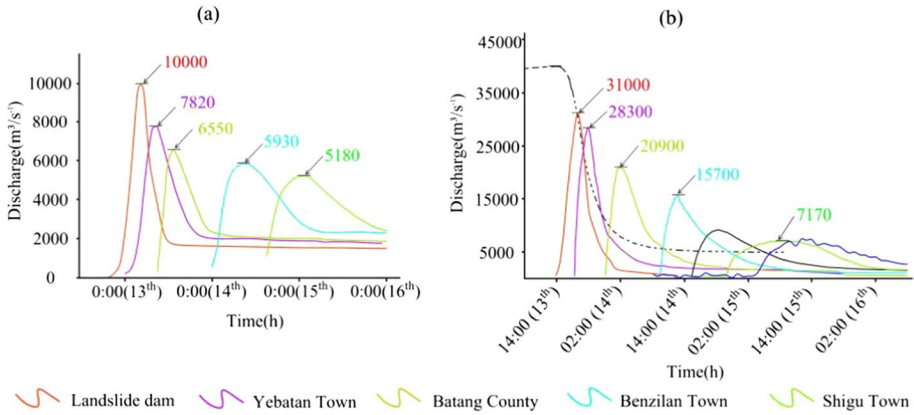
Fig. 9 Dam downstream outburst hydrographs. **a** First dam breach: October 2018. **b** Second dam breach: November 2018; here, the black dotted line represented the water level change of Boluo town 20 km upstream of the dam

**Fig. 10** Potential peak discharge attenuation downstream of the dam
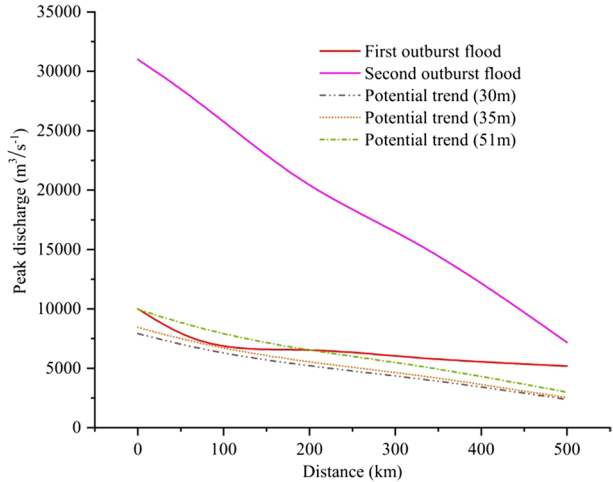
visualization. Because the landslide dam breaching process was slow, the flood process lasted a long time; whilst the study area was only 9 km long, the flood lasted more than 13 h. The peak discharge time was at 10800 s (Figs. 15 and 16). As shown in Fig. 15, the maximum flood depth was about 27 m at 10,800 s, and it then sharply decreased to 15 m by 43,200 s. As shown in Fig. 16, the largest flood velocity occurred during the peak discharge stage of 10,800 s and reach up to ~ 19 ms^{-1}. Most of the flood discharges are below 16 ms^{-1}, but there are locally high velocities due to a bedrock valley constraint. The maximum flood inundation at the 10,800 s stage is shown in Figs. 15 and 16.
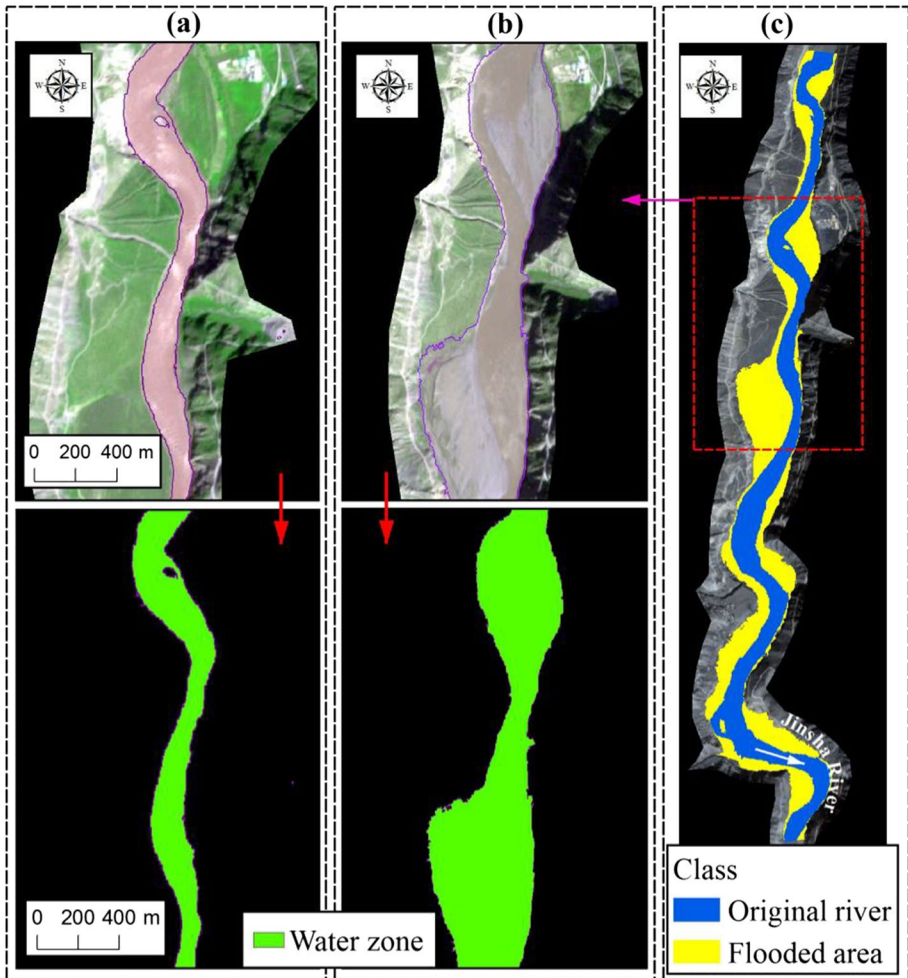
Fig. 11 November dam outburst flood illustrating the active zone of the river before the flood (**a**), after the flood (**b**), and the estimated flood area that results (**c**)

4.4 Upstream impacts of different landslide dam scenarios

The 30 m, 35 m, and 51 m dam height scenarios induce a storage capacity up to 142×10^6 m^3, 182×10^6 m^3, and 331×10^6 m^3, with the back-flow extending upstream by 32 km, 40 km, and 50 km, respectively (Table 4 and Fig. 17). The potential flooded area upstream of these dams is 5.0 km^2, 6.1 km^2, and 9.1 km^2, respectively (Table 4). Compared with the two landslide dam flood events of October and November 2018, the flooded area and back-flow distance of the potential events are lower, but the impacts would be no less serious. Take Boluo Town as an example, located 20 km upstream of the landslide dam, the 2018 floods inundated the whole town. The scenario of the 51 m dam height will also inundate the whole town (Fig. 17). There is a nonlinear relationship between the storage capacity and the inundated area, which reflects the form of the
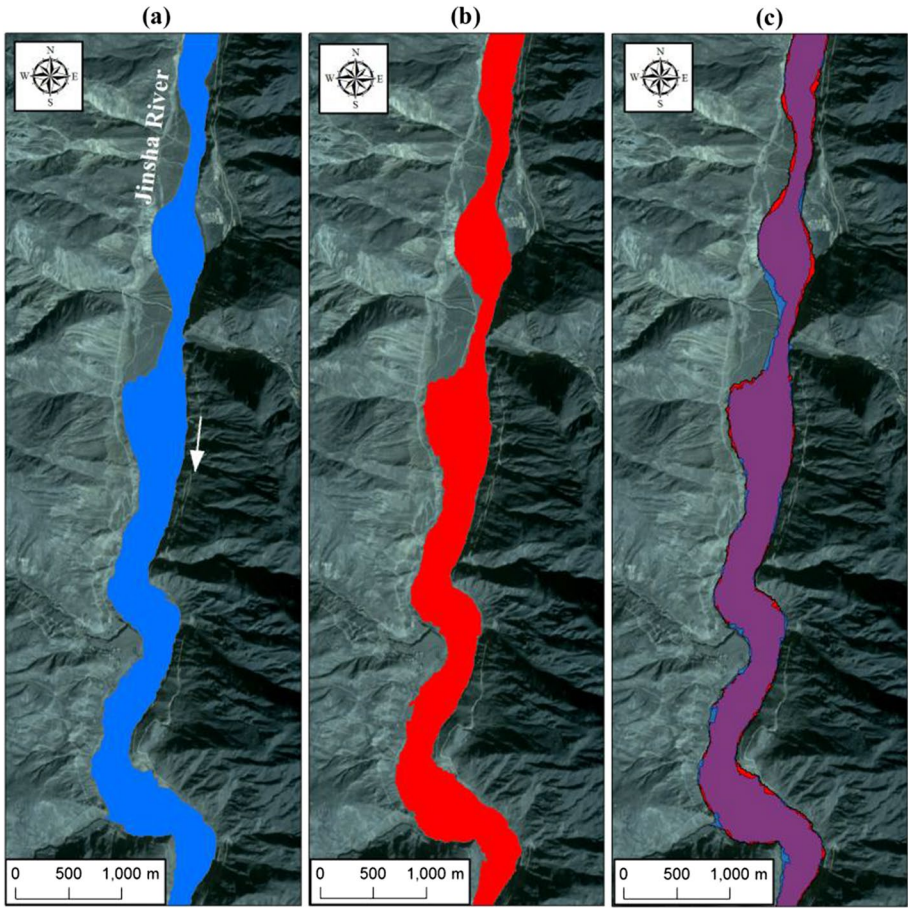
Fig. 12 Flood extent measured using remote sensing (**a**), modelled (**b**), and difference between the two (**c**)
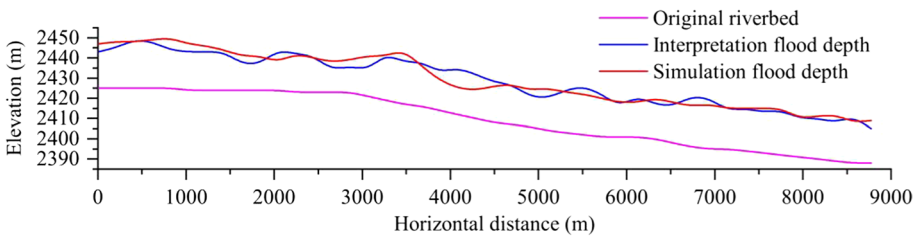
Fig.13 Flooded depth difference between the interpretation and the simulation result

valley upstream of the Baige landslide (Fig. 18). The increasing velocity of the flooded area is greater than the storage capacity (Fig. 18).
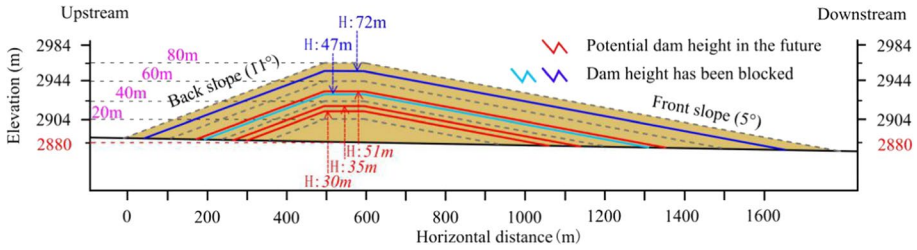
Fig. 14 Potential dam heights caused by future blockage by the Baige landslide

4.5 Outburst flood impacts downstream of the simulated dams

Following from the peak discharge calculation and application of attenuation, the peak discharges at the study area located at Batang county reach are 5300 m³s⁻¹, 5644 m³s⁻¹, and 6664 m³s⁻¹ for dam heights 30 m, 35 m, and 51 m, respectively. The BASEMENT simulation results show that the potential flood areas are 0.18 km², 0.34 km², and 0.43 km² on both sides of the river under the three different dam height scenarios (Fig. 19). These compare with a proportionately much higher flooded area for the inundated area of the 72 m height dam failure in November 2018, and this reflects the fact that the inundated width of the floodplain increases markedly for the discharges associated with the higher case (Fig. 20).
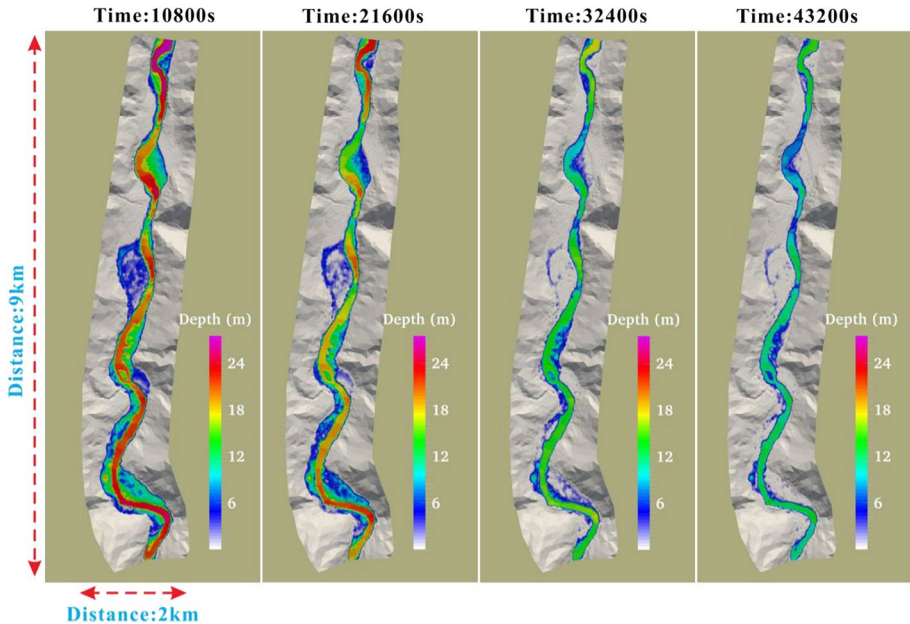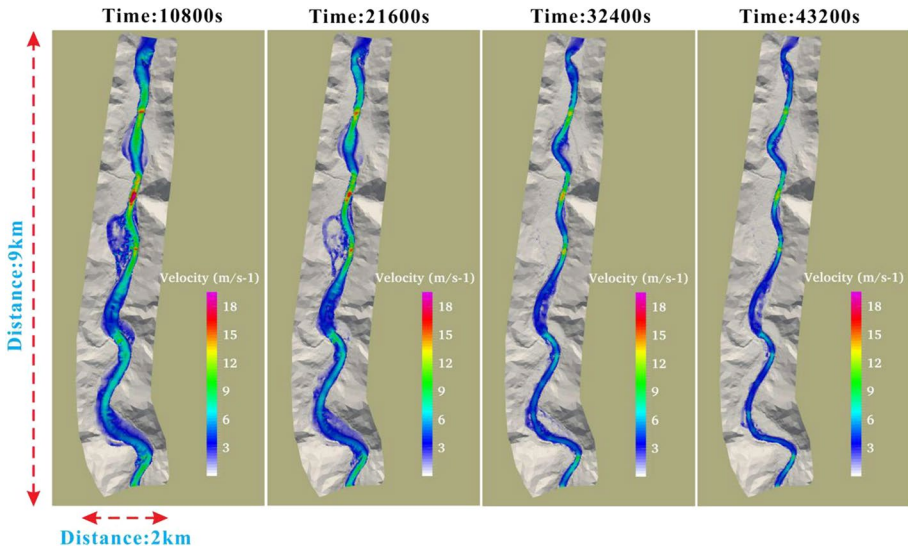

Fig. 15 Outburst flood depth evolution process based on the BASEMENT model

Fig. 16 Outburst flood velocity evolution process based on the BASEMENT model

5 Discussion

The Baige landslide is continuously deforming due to gravity, and this resulted in landslide dams that breached on two closely spaced dates in 2018 (Fan et al. 2020d; Chen et al. 2021a, b; Liu et al. 2021; Yang et al. 2021). The potentially unstable slope continues to erode and is likely already blocking the Jinsha River again. This paper, using the Baige landslide as a case study, focussed on quantifying how the dam drives inundation both upstream and downstream of the dam, the former due to storage of water upstream, and the latter due to an outburst flood with impacts downstream. Remote sensing was combined with the hydrodynamic model BASEMENT to estimate flood extent and with a good agreement between measurements and model predictions (Figs. 12, 13) reflected in Kappa value > 0.9. This approach was aided by high quality remotely sensed imagery for validation. The BASEMENT modelling, however, is crucially dependent upon estimates of the size of the flood discharge and hence, dam heights, the liberation of water during failure and attenuation of the discharge wave as it moves downstream.

Table 4 Dam upstream potential landslide dam disasters. The table shows data for the measured 2018 events and the three simulated dam heights

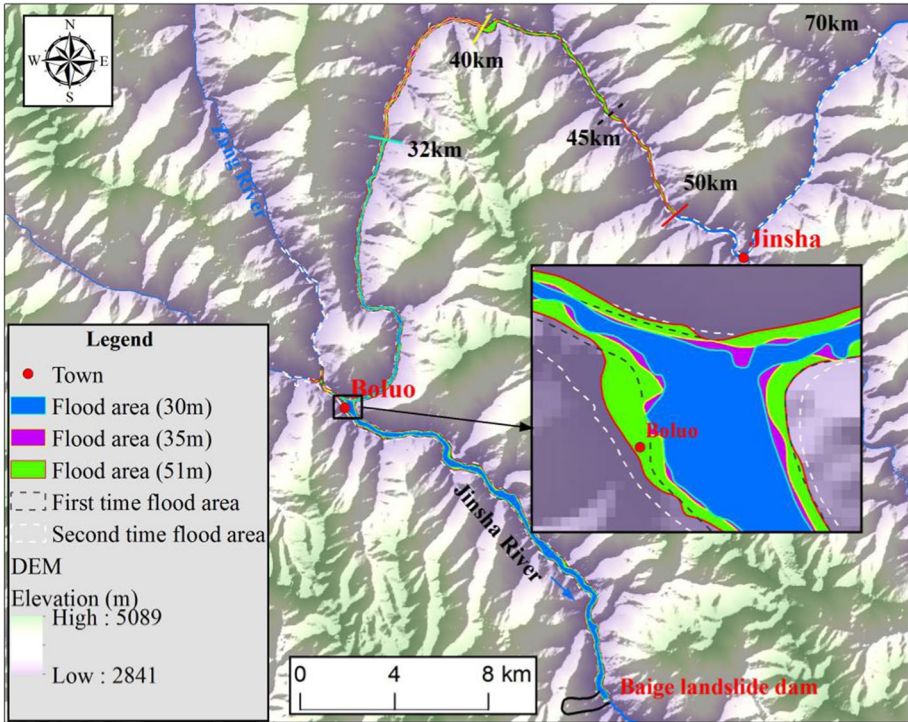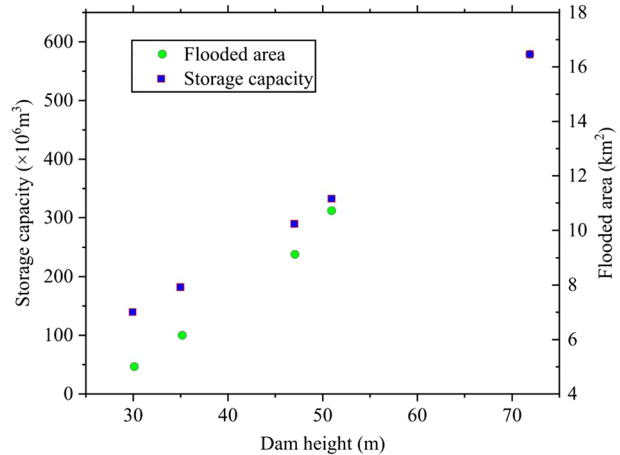| Dam height (breach, m)	Dam volume ($\times 10^4 m^3$)	Storage capacity ($\times 10^6 m^3$)	Flooded area (km²)	Back-flow distance (km)
30	130	142	5.01	32
35	260	182	6.12	40
47 measured	1800	290	9.1	45
51	590	331	10.75	50
72 measured	630	580	16.43	70

**Fig. 17** Upstream inundation extent for different dam heights

Fig. 18 Dam height, storage capacity, and dam volume relation upstream

First, the potential dam heights were impacted by the dam shape, dam breach deposit volume, and landslide volume. Based upon the landslide accumulation process, the dam shape and dam breach deposit size are easily determined after the breach. However, accurately determining landslide volume before the breach is harder. The volume calculation appeared distinct differences between different scholars even in the failed Baige landslide

events (Fan et al. 2020d; Xu et al. 2018; Chen et al. 2021a, b; Gao et al. 2021). Fan and Xu et al. (Fan et al. 2020d; Xu et al. 2018) calculated the Baige landslide volume to be ~30.0×10^6 m^3 in the first and 12.0×10^6m^3 in the second by superposing estimated topography before and after failure; Chen et al. (Chen et al. 2021a, b) calculated the volumes to be 27.0×10^6 m^3 in the first and 8.0×10^6m^3 in the second also using topographic superposition methods; Chen et al. (2021a, b), Gao et al. (2021) calculated the volumes to be 18.7×10^6 m^3 in the first and 6.3×10^6m^3 in the second using field measurements and before and after topographic superposition methods. The potential deformation range and unstable zones of the Baige landslide themselves have also differed according to the methods adopted (Fan et al. 2020d; Chen et al. 2021a, b). This work shows that the dam height has an important and nonlinear impact upon both upstream inundation (Fig. 18) and notably downstream outburst flood extent (Fig. 20), emphasising that determining the potential landslide volume and the form of the dam it produces is a key challenge for flood hazard assessment.

Second, the peak discharge is a critical driver of the outburst flood simulation. Although there is a long history in the application of empirical determinations of peak discharge, it is not clear that a universal model exists and that it is suitable for all landslides within a region let alone for all regions (Costa and Schuster 1988b, a; Walder and O'Connor 1997; Fread
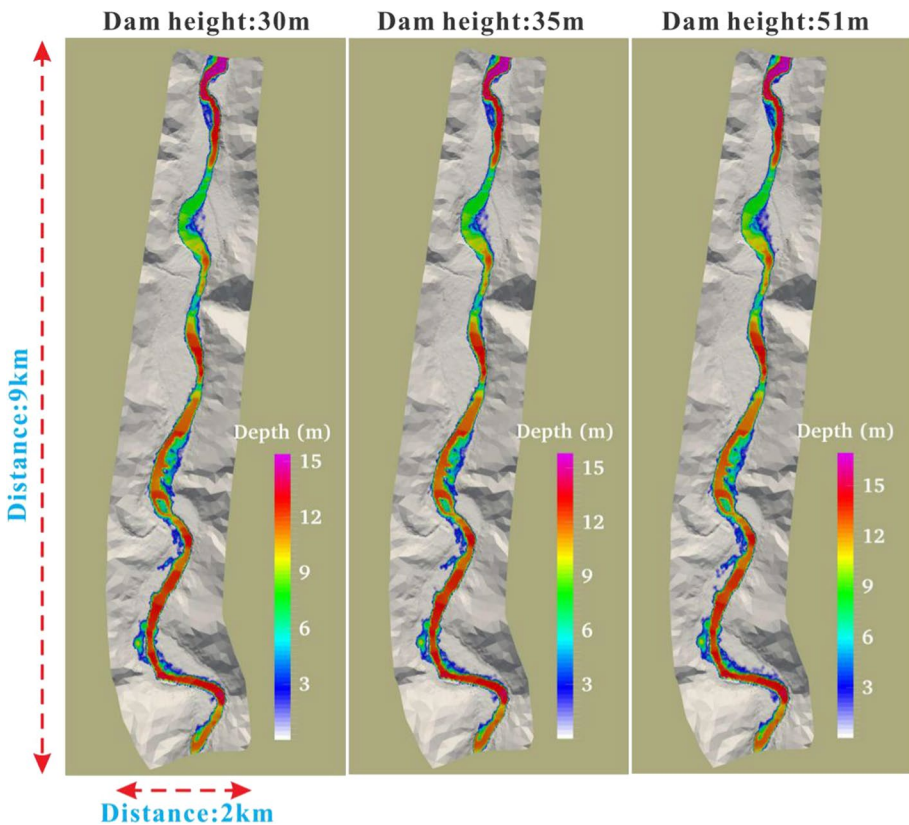
Fig. 19 Flooded area and water depth downstream for failure at different dam heights. Note that only one of the measured events is simulated

Fig. 20 Relation between dam height and potential inundated area for the study reach
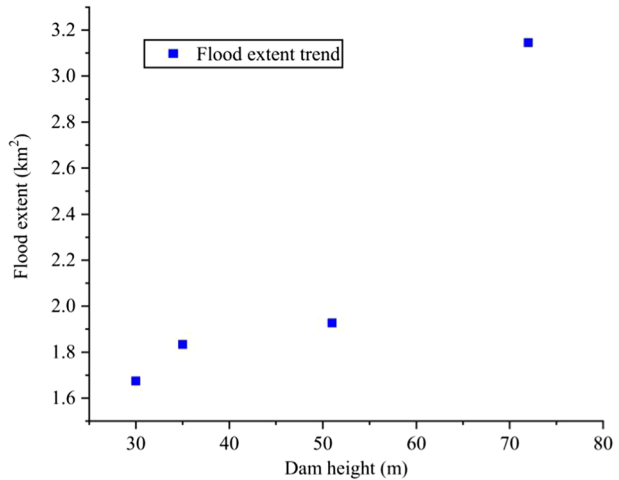
1988). Most empirical models only undertake simple fitting of geometrical parameters for different dams in a particular area and use few parameters (Costa 1985; Evans 1986; Cenderelli 2000; Pierce et al. 2010; Habib et al. 2014; Li et al. 2021). Many researchers have captured the geometry and size of landslide dams (such as dam volume, dam height, and breach depth and width) and barrier lakes (for example lake depth and storage capacity) to drive the empirical formula for calculating the peak discharge of the dam breaching (e.g. Evans 1986; Cenderelli 2000; Pierce et al. 2010; Liu et al. 2016 Fan et al. 2012). The dam height (or water depth), storage capacity, and breach size are very frequently used parameters. The dam height controls the storage capacity upstream, whereas the storage capacity exerts strong pressure on the dam and controlled the potential of the peak discharge (Cenderelli 2000; Pierce et al. 2010). Despite the size and shape of the dam breach being very effective parameters for calculating the peak discharge, they generally can only be determined reliably after the dam break. Fortunately, predictive models that represent the dam break process is now being developed based upon dam failure statistics, experiments, and numerical modelling (Peter et al. 2018; Xue et al. 2021), which could be used to calculate the peak discharge before the dam break. However, most of the models rarely consider dam materials and internal structures.

The estimations of peak discharge can be highly sensitive to the model used, as shown for the Baige landslide (Table 5). It implies that specific models need to be selected according to the specific study area. More challenging is the fact that the correct discharge height model may depend on landslide height. With only two landslide events available to calibrate such models, this uncertainty is extreme and a major weakness with the work presented in this paper. The model of Peng and Zhang (2012) is appropriate to calculate the potential peak discharge of the Baige landslide dam because it not only applied the geometry of the dam but also considered the erodibility of the dam. This model is based upon a large database of 1239 landslide dams and has been successfully applied to other sites (Rivas et al. 2015; Shi et al. 2017). A distinct deficiency is likely that the erodibility (a) value divided into high (1.236), medium (-0.380), and low (-1.615) needs a finer resolution formulation as well as further testing data. In this paper, we select the medium value (-0.380) as the erodibility (a) value because the Baige landslide is neither a soil landslide nor a rock landslide but somewhere between the two.

Third, the inundation extent downstream is not only a function of the magnitude of the dam breach but also the attenuation of the flood wave. In this case, empirical evidence suggested a relatively simple decline in peak discharge with distance downstream (Fig. 11) and little change in flood wave shape (Fig. 10). This facilitated the analysis. However, there is some evidence that the form of these decay curves (Figs. 10, 11) depends on the dam height with a more nonlinear decay in peak discharge with distance for the first and smaller of the two dam breach events. This suggests that hydraulic modelling of flood wave attenuation should be explored.

Finally, the BASEMENT model validation was surprisingly good given that the model had not been optimised against remotely sensed inundation extent. That said, there are a range of known impacts of hydraulic model parameters on flood extent, notably roughness (e.g. Yu and Lane 2006) as represented here by the Manning friction coefficient, and also the quality of floodplain topography. As shown in Table 6, the choice of the Manning friction coefficient depended on the land-use types (Chow et al. 1988; Jeremy et al. 2015). The study area is located in the dry hot and deep valley segment of the Jinsha River. Meadow and bare land are the primary land covers, and the forest and infrastructure and covers are not extensive. According to the land-use type, we value the Manning friction coefficient as 0.3 (Table 2). Other research (e.g. Yu and Lane 2006) has shown that flood inundation predictions are relative insensitive to parameterizations of flood plain roughness; the specification of roughness in the channel, which determines the discharge at which out-of-bank flow starts, is much more important. The mesh used for model solution may also have a significant impact (Lala et al. 2018). Testing of mesh effects may be worthwhile, especially as these interact with model parameters and notably friction parameterization. A crucial finding of this work was that the relationship between dam height and downstream flood extent is likely to be nonlinear (Fig. 20) emphasising the importance of using hydrodynamic models for evaluating the downstream impacts of outburst flood events.

Table 5 Empirical models of the peak discharge calculation of the Baige first two landslides

Source	Empirical equation	Peak discharge (m^3/s^{-1})	
		Dam height 47 m	Dam height 72 m
Costa (1985)	$Q_P = 0.981(H_d V_l)^{0.42}$	17,707	28,339
Froehlich (1995)	$Q_p = 0.607(V_l^{0.295} H_w^{1.24})$	22,540	46,924
Evans (1986)	$Q_P = 0.72 V_l^{0.53}$	21,999	31,765
USBR(1982)	$Q_p = 19.1 H_w^{1.85}$	23,681	52,131
McDonald and Landridge Monopolis (1984)	$Q_p = 1.154(V_l H_w)^{0.412}$	17,282	27,413
Cenderelli (2000)	$Q_P = 3.4 V_l^{0.46}$	26,557	36,530
Pierce et al. (2010)	$Q_P = 1.9(H_d V_l)^{0.40}$	21,505	33,655
	$Q_P = 0.0176(H_d V_l)^{0.606}$	24,379	78,050
Peng and Zhang (2012)	$Q_P/(g^{1/2} H_d^{5/2}) = (H_d/H_r)^{-1.371}$ $(V_l^{1/3}/H_d)^{1.536} e^a$	9590	11,347
Measured		10,000	31,000

H_w = water depth (m); H_d = dam height (m); V_l = storage capacity ($\times 10^6 m^3$) (as shown in Table 3); H_r = Reference height (1.0); a is erodibility parameter (Peng and Zhang (2012)), here $a = 0.38$

Table 6 Land-use type corresponds to the manning coefficient

Parameter	Land-use type	Value
Manning coefficient	Farmland	0.035
	House	0.150
	Road	0.030
	Forest	0.100
	Meadow	0.030
	Alluvial flat	0.025

6 Conclusion

The Baige landslide dam has failed and twice-triggered severe outburst floods. Unfortunately, the Baige landslide is continuously deforming and continues to be a significant potential hazard. As such, it is representative of a wider set of known flood risk cases where the risk cascades from an initial event (e.g. a landslide that blocks a valley) through a secondary event (e.g. landslide breach) through to a downstream risk (e.g. flood inundation) that can be catastrophic. In this paper, we developed a coupled approach to evaluating this problem showing how it is both necessary and possible to couple analysis of a landslide, to estimation of the dam that it may form in the valley below, to estimation of inundation downstream if that dam then breaches. We tested it successfully on the Baige landslide DEM case and it would merit being tested for a wider number of cases. We emphasise that volume of sediment may produce empirical relationships for dam breaching and the likely outflow flood that results and application of a suitable hydrodynamic model. In terms of the latter, we showed that BASEMENT is an accurate and effective hydrodynamic model for simulating outburst flooding process, and associated scenarios can be used to assess future flood hazard. This was confirmed here by comparison with remotely sensed data.

Three key conclusions follow for the case study consider here. First, remote sensing showed that the second time the Baige dam breached, and it triggered an inundated area reaching up to 3.1 km^2 within a length 9 km of downstream river valley. Second, the Baige landslide is continuously deforming which implies a high probability of future outburst flood events. Third, there is some evidence that the relationships between landslide height and both upstream inundation extent and downstream outburst flood extent are nonlinear. This emphasises that the likely consequences of an outburst flood will depend upon the size of the landslide dam and also the time since the last failure event. This hypothesis could be a very major consequence for river valleys at risk of landslide dam (or other) outburst floods and so merits assessment in other cases.

Ethical statements This manuscript has not been published or presented elsewhere in part or in entirety and is not under consideration by another journal. I have read and understood your journal's policies, and we believe that neither the manuscript nor the study violates any of these. There are no conflicts of interest to declare.

References

An HC, Ouyang CJ, Zhou S (2021) Dynamic process analysis of the Baige landslide by the combination of DEM and long-period seismic waves. Landslides 18(5):1625–1639

Benz UC, Hofmann P, Willhauck G, Lingenfelder L (2004) Multi-resolution, object-oriented fuzzy analysis of remote sensing data for GIS-ready information. ISPRS J Photogramm Remote Sens 58:239–258

Bishop Y, Fienberg S, Holland P (1975) Discrete multivariate analysis: theory and practice. MIT Press, Cambridge

Bonnard C (2006) Technical and human aspects of historic rockslide dammed lakes and landslide dam breaches. Italian J Eng Geol Environ 1:21–30

Briaud JL (2008) Case histories in soil and rock erosion: woodrow wilson bridge, Brazos River meander, normandy cliffs, and new orleans levees. J Geotech Geoenviron Eng 134(10):1425–1447

Cenderelli DA (2000) Floods from natural and artificial dam failures. In: Wohl EE (ed) Inland flood hazards. Cambridge University Press, New York, pp 73–103

Chen F, Gao YJ, Zhao SY, Deng JH, Li ZL, Ba RJ, Yu ZQ, Yang ZK, Wang S (2021a) Kinematic process and mechanism of the two slope failures at Baige Village in the upper reaches of the Jinsha River, China. Bull Eng Geol Env 80(4):3475–3493

Chen Z, Zhou HF, Ye F, Liu B, Fu WX (2021b) The characteristics, induced factors, and formation mechanism of the 2018 Baige landslide in Jinsha River, Southwest China. Catena 203:105337

Chow VT, Maidment DR, Mays LW (1988) Applied hydrology. McGraw-Hill, New York

Chow VT, Maidment DR, Mays LW (2011) Applied hydrology. McGraw-Hill, New York

Cohen JA (1960) coefficient of agreement for nominal scales. Educ Psychol Measur 20(1):37–46

Costa JE (1985) Floods from dam failures. US Geol Surv Open-File Rep 85–560:54

Costa JE, Schuster RL (1988a) The formation and failure of natural dams. Geol Soc Am Bull 100(7):1054–1068

Costa JE, Schuster RL (1988b) The formation and failure of natural dams. Geol Soc Am Bull 100:1054–1068

Costa JE, Schuster RL (1991) Documented historical landslide dams from around the world. US Geol Surv Open-File Rep 91–239:486

Delaney KB, Evans SG (2015) The 2000 Yigong landslide (Tibetan Plateau), rockslide-dammed lake and outburst flood: review, remote sensing analysis, and process modelling. Geomorphology 246:377–393

Ding C, Feng GG, Liao MS, Tao PG, Zhang L, Xu Q (2021) Displacement history and potential triggering factors of Baige landslides, China revealed by optical imagery time series. Remote Sens Environ 254:112253

Ermini L, Casagli N (2003) Prediction of the behaviour of landslide dams using a geomorphological dimensionless index. Earth Surf Process Landf 28(1):31–47

Evans SG (1986) The maximum discharge of outburst floods caused by the breaching of man-made and natural dams. Can Geotech J 23:385–387

Evans SG, Delaney KB (2011) Characterization of the 2000 Yigong Zangbo River (Tibet) landslide dam and impoundment by remote sensing. Natural and artificial rockslide dams 543–559.

Everitt BS (1998) The cambridge dictionary of statistics. Cambridge University Press, Cambridge

Fan XM, Westen CJ, van, Xu Q, Gorum T, Dai FC, (2012) Analysis of landslide dams induced by the 2008 Wenchuan earthquake. J Asian Earth Sci 57:25–37

Fan XM, Scaringi G, Korup O, West AJ, Westen Cees JV, Tanyas H, Hovius N, Hales TC, Jibson RW, Allstadt KE, Zhang LM, Evans SG, Xu C, Li G, Pei XG, Xu Q, Huang RQ (2019)

Earthquake-induced chains of geologic hazards: patterns, mechanisms, and impacts. Rev Geophys 57(2):421–503

Fan XM, Dufresne A, Subramanian SS, Alexander S, Hermannsd R, Stefanelli CT, Hewitt K, Yunus AP, Dunning S, Capra L, Geertsema M, Miller B, Casagli N, John DJ, Xu Q (2020a) The formation and impact of landslide dams–State of the art. Earth Sci Rev 203:103116

Fan XM, Yang F, Subramanian SS, Xu Q, Feng ZT, Olga M, Peng M, Ouyang CJ, John DJ, Huang RQ (2020b) Prediction of a multi-hazard chain by an integrated numerical simulation approach: the Baige landslide, Jinsha River. China Landslides 17(1):147–164

Fread DL (1988) BREACH: an erosion model for earth dam failures. National Weather Service (NWS) Report, NOAA, Silver Spring, Maryland, USA.

Froehlich DC (1995) Peak outflow from breached embankment dam. J Water Resour Pl Manage 121:90–97

Gao YJ, Zhao SY, Deng JH, Yu ZQ, Mahfuzur R (2021) Flood assessment and early warning of the reoccurrence of river blockage at the Baige landslide. J Geog Sci 31(11):1694–1712

Guo CB, Yan YQ, Zhang YS, Zhang XJ, Zheng YZ, Li X, Yang ZH, Wu RA (2021) Study on the creep-sliding mechanism of the giant XIONGBA ancient landslide based on the SBAS-InSAR Method, Tibetan Plateau. China Remote Sensing 13(17):3365

Habib H, Vahid N, Alireza BA (2014) Genetic programming simulation of dam breach hydrograph and peak outflow discharge. J Hydrol Eng 757–768.

Hanson GJ, Simon A (2001) Erodibility of cohesive streambeds in the loess area of the midwestern USA. Hydrol Process 15(1):23–38

Jeremy DB, Gibson S, Takagi H, Imamura F (2015) On the need for larger manning's roughness coefficients in depth-integrated tsunami inundation models. Coast Eng J 57(2):1550005-1–1550005-13

Knapp S, Gilli A, Anselmetti FS, Krautblatter M, Hajdas L (2018) Multistage rock-slope failures revealed in lake sediments in a seismically active Alpine region (Lake Oeschinen, Switzerland). J Geophys Res Earth Surf 123(4):658–677

Köpfli P, Grämiger LM, Moore JR, Christof V, Susan LO (2018) The Oeschinensee rock avalanche, Bernese Alps, Switzerland: a co-seismic failure 2300 years ago? Swiss. J Geosci 111:205–219

Lala JM, Rounce DR, McKinney DC (2018) Modeling the glacial lake outburst flood process chain in the Nepal Himalaya: reassessing Imja Tsho's hazard. Hydrol Earth Syst Sci 22(7):3721–3737

Lane SN (1998) Hydraulic modelling in hydrology and geomorphology: a review of high resolution approaches. Hydrol Process 12(8):1131–1150

Li YS, Jiao QS, Hu XH, Li ZL, Li BQ, Zhang JF, Jiang WL, Luo Y, Li Q, Ba RJ (2020a) Detecting the slope movement after the 2018 Baige Landslides based on ground-based and space-borne radar observations. Int J Appl Earth Obs Geoinf 84:101949

Li J, Cao ZX, Cui YF, Fan XM, Yang WJ, Huang W, Alistair B (2021) Hydro-sediment-morphodynamic processes of the baige landslide-induced barrier Lake, Jinsha River. China J Hydrol 596:126134

Li YL, Chen AK, Wen LF, Bu P, Li KP (2020b) Numerical simulation of non-cohesive homogeneous dam breaching due to overtopping considering the seepage effect. Eur J Environ Civil Eng 1–15

Liu N, Yang QG, Chen ZY (2016) Hazard mitigation for barrier lakes. Changjiang press, Wuhan

Liu D, Cui Y, Wang H, Jin W, Wu CH, Nazir AB, Zhang GT, Paul AC, Chen HY (2021) Assessment of local outburst flood risk from successive landslides: case study of Baige landslide-dammed lake, upper Jinsha river, eastern Tibet. J Hydrol 599:126294

Liu XJ, Zhao CY, Zhang Q, Lu Z, Li ZH (2020a) Deformation of the Baige landslide, Tibet, China, revealed through the integration of cross-platform ALOS/PALSAR-1 and ALOS/PALSAR-2 SAR observations. Geophys Res Lett 47(3): e2019GL086142.

Liu W, Ju NP, Zhang Z, Chen Z, He SM (2020b) Simulating the process of the Jinshajiang landslide-caused disaster chain in October 2018. Bull Eng Geol Environ 1–11

McDonald TC, Langridge-Monopolis J (1984) Breaching characteristics of dam failures. J Hydraul Eng 110:567–586

Ouyang CJ, An HC, Zhou S, Wang ZW, Su PC, Wang DP, Cheng DX, She JX (2019) Insights from the failure and dynamic characteristics of two sequential landslides at Baige village along the Jinsha River. China Landslides 16(7):1397–1414

Peng M, Zhang LM (2012) Breaching parameters of landslide dams. Landslides 9(1):13–31

Peter SJ, Siviglia A, Nagel J, Marelli S, Boes RM, Vetsch D, Sudret B (2018) Development of probabilistic dam breach model using Bayesian inference. Water Resour Res 54:4376–4400

Pierce MW, Thornton CL, Abt SR (2010) Predicting peak outflow from breached embankment dams. J Hydrol Eng 15:338–349

Rivas DS, Somos-Valenzuela MA, Hodges BR, McKinney DC (2015) Predicting outflow induced by moraine failure in glacial lakes: the Lake Palcacocha case from an uncertainty perspective. Nat Hazards Earth Syst Sci 15:1163–1179

Shang YJ, Yang ZF, Li LH, Liu DA, Liao QL, Wang YC (2003) A super-large landslide in Tibet in 2000: background, occurrence, disaster, and origin. Geomorphology 54(3–4):225–243

Shang YJ, Park HD, Yang ZF, Yang J (2005) Distribution of landslides adjacent to the northern side of the Yarlu Tsangpo Grand Canyon in Tibet. China Environ Geol 48(6):721–741

Shi ZM, Xiong X, Ming P, Zhang LM, Xiong YF, Chen HX, Zhu Y (2017) Risk assessment and mitigation for the Hongshiyan landslide dam triggered by the 2014 Ludian earthquake in Yunnan, China. Landslides 14:269–285

USBR – US Bureau of Reclamation (1982) Guidelines for defining inundated areas downstream from Bureau of Reclamation dams, Reclamation Planning Instruction 82–11. Water Resources ResearchLaboratory, Denver, CO.

Vanzo D, Peter S, Vonwiller L, Bürgler M, Weberndorfer M, Siviglia A, Conde D, Vetsch DF (2021) BASEMENT v3: A modular freeware for river process modelling over multiple computational backends. Environ Model Softw 143:105102

Walder JS, O'Connor JE (1997) Methods for predicting peak discharge of floods caused by failure of natural and constructed earthen dams. Water Resour Res 33(10):2337–2348

Wang HJ, Zhou Y, Wang SX, Wang FT (2020) Coupled model constructed to simulate the landslide dam flood discharge: a case study of Baige landslide dam. Jinsha River Front Earth Sci 14(1):63–76

Wang SJ, Yang YD, Gong WY, Che YJ, Ma XG, Xie J (2021) Reason analysis of the Jiwenco glacial lake outburst flood (GLOF) and Potential Hazard on the Qinghai-Tibetan Plateau. Remote Sens 13(16):3114

Worni R, Stoffel M, Huggel C, Volz C, Casteller A, Luckman B (2012) Analysis and dynamic modeling of a moraine failure and glacier lake outburst flood at Ventisquero Negro, Patagonian Andes (Argentina). J Hydrol 444:134–145

Worni R, Huggel C, Stoffel M (2013) Glacial lakes in the Indian Himalayas—From an area-wide glacial lake inventory to on-site and modeling based risk assessment of critical glacial lakes. Sci Total Environ 468:S71–S84

Wu YB, Niu RQ, Lu Z (2019) A fast monitor and real time early warning system for landslides in the Baige landslide damming event, Tibet, China. Natural Hazards and Earth System Sciences Discussions 1–20.

Xiong ZQ, Feng GC, Feng ZX, Miao L, Wang YD, Yang DJ, Luo SR (2020) Pre-and post-failure spatial-temporal deformation pattern of the Baige landslide retrieved from multiple radar and optical satellite images. Eng Geol 279:105880

Xu Q, Shang YJ, van Asch T, Wang ST, Zhang ZY, Dong XJ (2012) Observations from the large, rapid Yigong rock slide–debris avalanche, southeast Tibet. Can Geotech J 49(5):589–606

Xu Q, Zheng G, Li WL, He MC, Dong XJ, Guo C (2018) Study on successive landslide damming events of Jinsha River in Baige Village on October 11 and November 3. J Eng Geol 26(6):1534–1551

Xue RY, Zhang XH, Cai YJ, Wang M, Deng Q, Zhang H, Kawaike K (2021) Numerical simulation of landslide dam overtopping failure considering headward erosion. J Hydrol 601:126608

Yang WT, Wang YQ, Sun S, Wang YJ, Ma C (2019) Using Sentinel-2 time series to detect slope movement before the Jinsha River landslide. Landslides 16(7):1313–1324

Yang ZK, Wei JB, Deng JH, Gao YJ, Zhao SY, He ZL (2021) Mapping outburst floods using a collaborative learning method based on temporally dense optical and SAR data: a case study with the Baige landslide dam on the Jinsha river. Tibet Remote Sens 13(11):2205

Yu D, Lane SN (2006) Urban fluvial flood modelling using a two-dimensional diffusion-wave treatment, part 1: mesh resolution effects. Hydrol Process Int J 20(7):1541–1565

Zhang SL, Yin YP, Hu XW, Wang WP, Zhang N, Zhu SN, Wang LQ (2020) Dynamics and emplacement mechanisms of the successive Baige landslides on the Upper Reaches of the Jinsha River. China Eng Geol 278:105819

Zhang SL, Yin YP, Hu XW, Wang WP, Li ZL, Wu XM, Luo G, Zhu SN (2021) Geo-structures and deformation-failure characteristics of rockslide areas near the Baige landslide scar in the Jinsha River tectonic suture zone. Landslides 18(11):3577–3597

Zhou JW, Cui P, Hao MH (2016) Comprehensive analyses of the initiation and entrainment processes of the 2000 Yigong catastrophic landslide in Tibet. China Landslides 13(1):39–54

Zhou S, Ouyang CJ, Huang Y (2022) An InSAR and depth-integrated coupled model for potential landslide hazard assessment. Acta Geotechnica 1–20.

Zischg AP, Galatioto N, Deplazes S, Weingartner R, Mazzorana B (2018) Modelling spatiotemporal dynamics of large wood recruitment, transport, and deposition at the river reach scale during extreme floods. Water 10(9):1134